Extraction of Molecular-Frame Electron-Ion Differential Scattering Cross Sections Based on Elliptical Laser-Induced Electron Diffraction

Yizhang Yang,[1,*] Xiaoqing Hu,[2,*] Lu Wu,[1,*] Zhenpeng Wang,[3,2] Xiaokai Li,[1] Shengpeng Zhou,[1] Zhenzhen Wang,[1] Fuming Guo,[1] Lanhai He,[1] Sizuo Luo,[1] Dongdong Zhang,[1] Jianguo Wang,[2] Xiangjun Chen,[3] Yong Wu,[2,†] Chuncheng Wang,[1,‡] and Dajun Ding[1,§]

[1]*Institute of Atomic and Molecular Physics, Jilin University, Changchun 130012, China*
[2]*National Key Laboratory of Computational Physics, Institute of Applied Physics and Computational Mathematics, Beijing 100088, China*
[3]*Department of Modern Physics, University of Science and Technology of China, Hefei, Anhui 230026, China*

We extracted the molecular-frame elastic differential cross sections (MFDCSs) for electrons scattering from N_2^+ based on elliptical laser-induced electron diffraction (ELIED), wherein the structural evolution is initialized by the same tunneling ionization and probed by incident angle-resolved laser-induced electron diffraction imaging. To establish ELIED, an intuitive interpretation of the ellipticity-dependent rescattering electron momentum distributions was first provided by analyzing the transverse momentum distribution. It was shown that the incident angle of the laser-induced returning electrons could be tuned within 20° by varying the ellipticity and handedness of the driving laser pulses. Accordingly, the incident angle-resolved DCSs of returning electrons for spherically symmetric targets (Xe^+ and Ar^+) were successfully extracted as a proof-of-principle for ELIED. The MFDCSs for N_2^+ were experimentally obtained at incident angles of 4° and 7°, which were well reproduced by the simulations. The ELIED approach is the only successful method so far for obtaining incident angle-resolved ionic MFDCS, which provides a new sensitive observable for the transient structure retrieval of N_2^+. Our results suggest that the ELIED has the potential to extract the structural tomographic information of polyatomic molecules with femtosecond and subangstrom spatiotemporal resolutions that can enable the visualization of the nuclear motions in complex chemical reactions as well as chiral recognition.

Capturing the structural evolution of molecules at the atomic length and timescales can bridge their structure and functionality, and plays an essential role in physics, chemistry, and biology [1–3]. Many ultrafast imaging techniques have been developed to achieve the ultrafast imaging of gaseous or crystal targets with subangstrom accuracy, such as ultrafast electron diffraction (UED) [4–7], laser-induced electron diffraction (LIED) [8,9], x-ray diffraction with free-electron laser [10,11], and Coulomb explosion imaging [12,13]. Ultrashort electron bunches have been proposed to directly determine the structural changes during a photochemical reaction, and the reaction is pumped by femtosecond laser pulses and probed via mega-electron-volt electron diffraction imaging [14,15]. Currently, this technique can achieve a temporal resolution of 50 fs [16]. A similar temporal resolution can be achieved by x-ray diffraction and Coulomb explosion imaging [17–20]. Based on the strong-field tunneling ionization process, the tabletop LIED technique can increase the temporal resolution further to the femtosecond or subfemtosecond level through the intracycle pump-probe scheme [21–24]. The ultrafast motion of a proton within a gaseous molecule has been visualized at this unprecedented temporal resolution [25]. The subcycle tunneling ionization was used as a pump to initiate the dynamics of an isolated molecule, and the ionized electron was driven back to collide with the parent ion by the oscillating electric field. The elastic scattering differential cross sections (DCSs) of laser-induced returning electrons by the parent ion can be extracted from the measured momentum distributions of high-energy rescattering electrons, and the transient structure of the parent ion can be extracted from the measured DCSs. With LIED, the DCSs for various molecules have been extracted, where the direction of the returning electron is parallel to the polarization direction of driving laser (i.e., incident angle of 0°) [26–29]; furthermore, the alignment-dependent electron diffraction image of neutral molecules has been obtained with an electron diffraction technique in combination with ultrashort laser pulse [30–32]. However,

---

[*]These authors contributed equally to this work.

[†]Contact author: wu_yong@iapcm.ac.cn

[‡]Contact author: ccwang@jlu.edu.cn

[§]Contact author: dajund@jlu.edu.cn
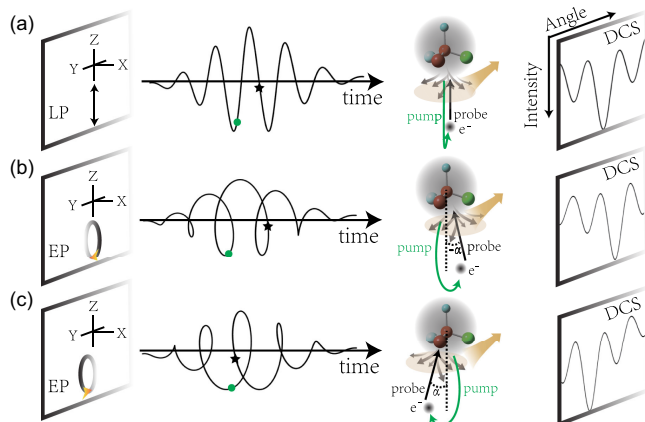
FIG. 1. (a) Schematic of LIED. An electron ionized from an oriented molecule at an instant (green dot in the electric field) returns to the parent ion and is scattered off by this molecule (black star). The incident angle is 0° relative to the laser polarization direction. The right panel presents a typical DCS. (b),(c) Schematics of ELIED with opposite helicities of the driving laser pulse. An electron is ionized and scattered at the same time instant with LIED, the incident angle is changed to $\pm\alpha$ and the different DCSs are obtained. This enables tomographic structural imaging of the target.

the incident angle-resolved DCSs of molecular ions in the molecular frame have not yet been experimentally obtained with LIED or UED. By tuning the incident angle of the probing electron beam, different molecular-frame differential cross sections (MFDCSs) scattered by the same transient molecular ion can be obtained, which can be used to extract the tomographic imaging of complex molecules (see Fig. 1).

Here, the incident angles of laser-induced returning electrons driven by different elliptical laser pulses were first established by analyzing the transverse momentum distributions of rescattering electrons (TMDE). The DCSs at different incident angles for spherically symmetric atoms were extracted to verify the elliptical laser-induced electron diffraction (ELIED) approach. Furthermore, the MFDCSs at incident angles of 0°, 4°, and 7° for prototype molecules (N_2^+) were obtained, which demonstrates that ELIED is so far the only feasible approach for obtaining incident angle-resolved ionic MFDCS.

The experimental setup [33] is described in Supplemental Material (SM) [34]. Figure 1 presents a schematic of LIED and ELIED. One electron was liberated from a spatially oriented molecule through tunneling ionization; this electron then accelerated and returned to the vicinity of the parent ion in the oscillating electric field. The returning electron can be scattered off by its parent ion at approximately 2 fs (three-quarters of the optical cycle) after tunneling ionization, and the DCS can be extracted [41–43]. For LIED, the returning electron propagates along the laser polarization direction; thus, the incident angle for the returning electron is defined as 0° in the laboratory coordinate system [see Fig. 1(a)]. In the case of ELIED, the rescattering electron trajectory is affected

by the vector potential along the minor axis of the elliptical laser pulse. The incident angle of the returning electron varies relative to the major axis direction, which can be controlled by changing the ellipticity [see Fig. 1(b)]. Thus, we can obtain several DCSs by probing the same transient structure of the molecule at different incident angles; this allows us to reconstruct the transient structure topographically. Interestingly, the elliptical laser-induced returning electron acquires a helical trajectory owing to the influence of the magnetic field when the nondipole effect is included, and the helicity of the returning electron trajectory is defined by the handedness of the driving laser pulse [44]. Thus, a chiral response can arise as the DCSs of the returning electron with different helicity by one enantiomer are different, as shown in Figs. 1(b) and 1(c). Moreover, the laser-induced returning electron beam in ELIED can recollide in deep regions in the ionic core of chiral molecules and is expected to be very sensitive to the chiral molecular potential [45]. Thus, ELIED can have applications for chirality discrimination of gas-phase chiral molecules.

However, to establish ELIED, an intuitive interpretation of the ellipticity-dependent rescattering electron distributions is necessary. In the elliptical laser field, it is formidable to theoretically disentangle the dynamics of returning electrons in the polarization plane because of the presentation of both the laser field and the Coulomb potential of the ionic core [46]. Interestingly, in the light-propagation direction, the electrons are only affected by the Coulomb potential within the dipole approximation; thus, the transverse momentum distribution (TMD) can accurately reflect the interaction between the returning electron and the ionic core at different ellipticities [37].

To establish the incident angles of the returning electron driven by the elliptical laser pulse, we first studied the strong-field tunneling ionization of the Xe atom and presented the TMDE for ellipticities in the range of 0–0.3 in Figs. 2(a)–2(d). For each point in the polarization plane (that is, each combination of the p_z and p_y components), the TMD were fitted with a Lorentzian distribution, and the half width at half maximum (HWHM) of the TMD can be obtained from the fit [37]. The returning electrons can be attracted by the Coulomb potential of the parent ion, thus leading to the reduction in transverse velocity and narrowing of the profile of the TMD (Coulomb focusing effect) [38]. The most prominent rescattering electron distributions in Fig. 2(a) are the nodal structures located at 0° (main node) and $\pm25°$ (side nodes), which are the well-known diffraction patterns of LIED for Xe driven by the linearly polarized field [47,48]. Interestingly, the side nodes have much larger HWHM values than the main node. The one-dimensional distribution of the main and side nodes [integrated along the black curves in Figs. 2(a)–2(d) with $p = 1.45$ a.u.] is shown as the solid black curve in Fig. 2(e). Moreover, as the ellipticity increases from 0.1 to 0.3, the distribution of HWHM changes gradually [see Figs. 2(b)–2(d)], and their
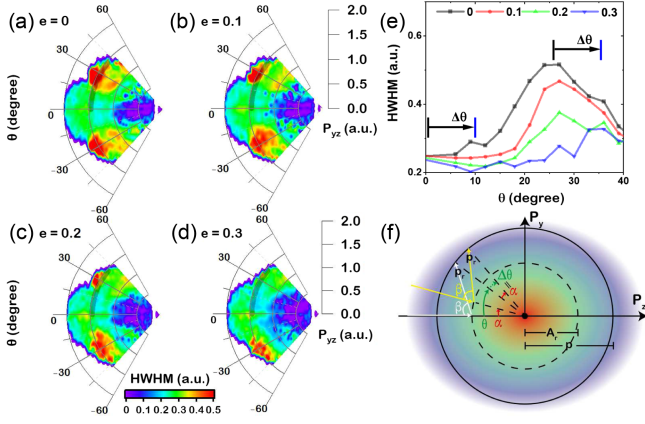
FIG. 2. (a)–(d) HWHM of TMDE ionized from Xe atom for laser ellipticities from 0 to 0.3. The values of the HWHM are encoded in the color scale. (e) One-dimensional angular-dependent distributions of HWHM from the black curves ($p = 1.45$ a.u.) in Figs. 2(a)–2(d). $\Delta\theta$ indicates the angular offset for ellipticity values in the range of 0–0.3. (f) Schematic of electron elastic rescattering driven by laser pulses with different ellipticity values analogous to classical Rutherford scattering. θ is the detected angle relative to the P_z in the momentum frame, and α is the incident angle offset for the returning electron driven by elliptical laser pulses, and the collision center rotates along the circle with the momentum of A_r. In this model, α is equal to $\Delta\theta$.

one-dimensional distributions show that the position of the maximum HWHM for side nodes shifts from approximately 25° to 35° as the ellipticity increases from 0 to 0.3, and the position of the minimum HWHM for the main node also shifts to a larger angle (for example, approximately 10° for 0.3). In the following, we show the correspondence between this angular shift of the maximum position of HWHM to the incident angle of the returning electron for each ellipticity of the driving pulse within the classical scattering model.

In the elliptical laser field, the incident direction of the returning electron may shift away from the direction of the major axis because of the existence of the vector potential perpendicular to the major axis during its propagation. According to the quantitative rescattering (QRS) theory [47–49], the rescattering electron in the "back-rescattered ridges" (BRR) can be expressed as $\hat{p} = \hat{A}_r + \hat{p}_r (A_r = p_r/1.26)$, where the first term signifies the momentum gained as the electron propagates from the moment of backscattering to the end of the laser pulse ($\hat{A}_r$ represents the vector potential, whose magnitude is linked to the effective ponderomotive energy through the equation $U_p = A_r^2/4$), the second term depicts the backscattering of the electron into the direction of $\hat{p}_r$ ($\hat{p}_r$ is related to the effective ponderomotive energy through the equation $3.17U_p = p_r^2/2$). Here, the collision center was located at $A_r = 0.76$ a.u., and the incident angle was 0° in the case of linear polarization. The typical trajectory forming the side node is shown by the white arrow in Fig. 2(f). For the

elliptical laser field, we assume that the elastic electron-ion collision is analogous to the classical Rutherford scattering [50], and reveal the value of α according to the ellipticity-dependent TMDE. In this model, the momentum transfer between the electron and the ionic core can be described by the impact parameter $b = (a/2)ctg[(180° - \beta)/2]$, where $a = 2m_e e^2/4\pi\varepsilon_0 p^2$, $p_r \sin\beta = p \sin(\theta - \alpha)$. The larger momentum transfer (smaller b) indicated a stronger inter-action between the electron and the ionic core, which led to a stronger Coulomb focusing effect, that is, a smaller HWHM in Fig. 2. According to this equation, larger scattering angles ($180° - \beta$) correspond to smaller b values. The main node in Fig. 2(a) is formed by trajectories with a scattering angle of 180°, thus resulting in a smaller HWHM than that of the side node (with a scattering angle less than 155°). With this model, we can qualitatively explain the observed difference in HWHM between the main and side nodes in Fig. 2(e). Furthermore, this equation also suggests that the incident angle α can be accurately mapped to the angular offset of impact factors [also see Fig. 2(f)], thus the observed angular offset ($\Delta\theta$) of HWHM for the main node and side node in Fig. 2(e) can also reflect the changes in α for the returning electron in the elliptical field, as indicated by the yellow arrow in Fig. 2(f). The α for the ellipticity values of 0.1, 0.2, and 0.3 are approximately equal to 2°, 5°, and 10°, respectively.

By establishing the incident angle of the returning electron in the elliptical laser field, the DCS could be obtained in the rotated ion-electron collision coordinates. For linearly polar-ized light, the DCS of the returning electron ($p_r = 0.95$ a.u., $E = 12$ eV) could be extracted directly from the momentum distribution [see Fig. 3(a)] based on the QRS theory, as shown by the red dots in Fig. 3(e). We calculated the DCS of Xe^+ for a free electron using the distorted wave method [51], where the DCS is proportional to the scattering matrix element $\|\langle k\|V\|\psi\rangle\|^2$. Herein, k represents the plane wave of the rescattering electron, V is the electron-ion distortion potential, and ψ is the distortion wave calculated by solving the Schrödinger equation $E_0\psi = [-(\nabla^2/2\mu) + V]\psi$. The Coulomb interaction, polarization, and electron exchange interactions [52] were accurately considered in calculations. The results are plotted in Fig. 3(e). A good agreement between the extracted DCS and simulation could be reached. Those results were consistent with the literature [47,48]. For a spherically symmetric atom, varying α will not change the DCS; thus, the same DCS should be obtained for ELIED. Based on this argument, we tuned the α and obtained the DCSs from Figs. 3(b)–3(d). The most probable values of α are shown in Figs. 3(e)–3(f), where the best agreements between the DCSs in the elliptical (green-dotted lines) and the linear cases (red-dotted line) are obtained. We can see that these DCSs are consistent when α has values 2°, 4°, and 10° for ellipticities of 0.1, 0.2, and 0.3, respectively. These incident angles are the same within the error as the values
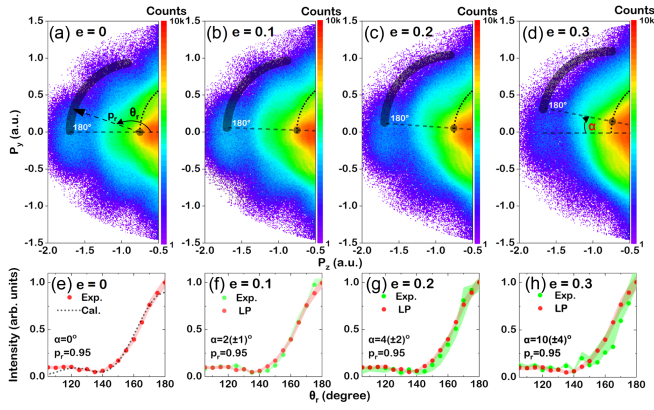
FIG. 3. (a)–(d) Momentum distributions of rescattering electrons for Xe driven by the laser pulse at the ellipticities of 0, 0.1, 0.2, and 0.3, respectively. The electrons in low-energy regions are masked to emphasize the structure of high-energy electrons. The solid black lines stand for the BRR. The momentum of returning electron p_r and scattering angle θ_r are indicated using arrows in (a). The DCS extracted from (a) is shown in (e) (Exp.) and normalized at 170° to the calculations (Cal.) for comparison. (f)–(h) The green dots with shading errors are the DCSs obtained from (b)–(d), respectively. The DCS from linearly polarized light (LP, red dot) are inserted for comparison.

obtained from the analysis of TMD. This agreement confirms that the incident angle of the returning electron can be controlled within 20° by tuning the ellipticity and the handedness of the driving laser pulse. The extracted incident angle-resolved DCSs for spherically symmetric targets can serve as proof of principle for the validity of ELIED.

We applied ELIED to the mixtures of Ar and N_2, and their rescattering electron momentum distributions are presented in Figs. 4(a)–4(c) and 4(e)–4(g) with ellipticity of 0, 0.2, and 0.3, respectively. Ar and N_2 have similar ionization potentials, and the results of Ar can serve as a reference to emphasize the molecular structural sensitivity of ELIED. Here, N_2 is aligned to the direction of the main axis of the elliptical laser pulse; moreover, the strong field tunneling ionization of N_2 has the highest yield when the N-N axis is parallel to the laser polarization direction because of its typical σ orbital [53,54]. Thus, in the ELIED, the returning electrons with different incident angles can be scattered by this aligned transient N_2^+, and the incident angle-resolved MFDCSs can be extracted. The DCSs from Ar^+ can be extracted from the electron momentum distributions [Figs. 4(a)–4(c)] using the same procedure as that used for Xe; the results are shown in Fig. 4(d). The extracted DCS of Ar^+ driven with the linearly polarized laser pulse was compared with the calculated DCS obtained from distorted wave calculations, the overall reasonable agreement can be reached. The discrepancies around 105° may originate from the "contamination" of direct ionized electrons [47,48]. Applying the same method to Ar as that used for Xe in ELIED, consistent DCSs were extracted in the case of elliptical laser pulse (ellipticity is 0.2 and 0.3) by
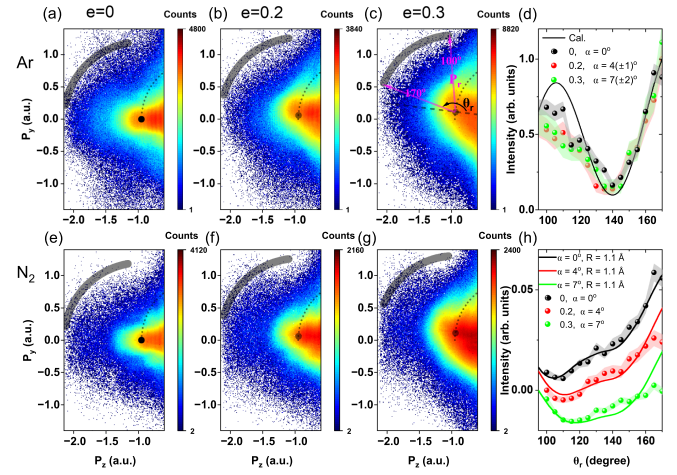
FIG. 4. (a)–(c) and (e)–(g) Momentum distributions of rescattering electrons ionized from Ar and N_2 driven by the laser pulse at the ellipticities of 0, 0.2, and 0.3, respectively. α stands for the angular shift of the incident angle relative to the polarization direction of linear laser pulse. (d) Extracted DCSs for Ar in the case of the linearly (black ball) and elliptically polarized pulses (red ball and green ball). The calculated DCS is shown as a black solid line which are normalized with experiment at 155° of θ_r for comparison. Herein, the α is estimated to be 4° and 7° ($p_r = 1.2$ a.u., $E = 20$ eV) with the ellipticity of 0.2 and 0.3, respectively. Accordingly, (h) presents the extracted and calculated MFDCSs for N_2^+ as α is 4° and 7° ($p_r = 1.3$ a.u., $E = 23$ eV). The measured and simulated results are also normalized at 155°. The red and green curves are offset by 0.01 and 0.025, respectively for clarity.

tuning the incident angle of the returning electron beam to 4° and 7°, respectively.

The incident angle of returning electron for N_2^+ in the same elliptically polarized pulse is assumed to be identical as Ar^+ when the difference between their Coulomb potential is ignored. At first, the DCS of the returning electron by N_2^+ in the case of linearly polarized laser pulse was extracted [see black ball in Fig. 4(h)], and the calculated MFDCS at the incident angle of 0° was inserted for comparison using the modified molecular multicenter three-distorted-wave calculation [55], as indicated by the black solid line in Fig. 4(h). Here, the equilibrium bond length of N_2 (1.10 Å) is used. The experimentally extracted and calculated MFDCSs both present a minimum at around 110° and a hump around 100°, and the dominant peak appears for largest angle. In the case of the elliptically polarized laser pulses, the MFDCSs were directly extracted by setting the incident angle to 4° and 7° as the ellipticity is 0.2 and 0.3, respectively [see Fig. 4(h)]. The simulated MFDCSs with the same incident angle well reproduced the experimental results, which demonstrates the incident angle-resolved MFDCS for the molecular system can be obtained with the ELIED. Moreover, the MFDCSs exhibit prominent incident angle-resolved features. As increasing the incident angles, the position of the minimum shifted to

the larger angle and the hump at 100° becomes higher, in contrast, the amplitude for the dominant peak at larger angles decreases. Those incident angle-resolved features can offer a new observable to retrieve the bond length. We define the amplitude ratio between the hump at 100° and the minimum for incident angle, and this ratio shown in Fig. S6 (in Supplemental Material [34]) becomes larger as increasing the incident angle. To retrieve the transient bond length of N_2^+, we simulated the MFDCSs with bond length from 1.00 Å to 1.20 Å in 0.02 Å increments, and they show drastically different MFDCSs and ratios (see Figs. S5 and S6), indicating that the ELIED can provide angle-resolved probing of the transient structure of ion with subangstrom resolution in the molecular frame. Here, we reveal that the most probable transient bond length of N_2^+ is 1.11 Å within a fitting error range of 1.10 to 1.16 Å. Moreover, three measurements with different incident angles show that the precision of the current approach for transient bond length can reach to 0.01 Å (see discussions in Sec. V of Supplemental Material [34]). Those results can facilitate the tomographic imaging of complex transient molecular structures.

In conclusion, we proposed an ultrafast molecular imaging approach (ELIED) based on the intracycle pump-probe scheme. We experimentally extracted the MFDCSs of N_2^+ with ELIED, where the incident angles of returning electron beam were tuned by varying the ellipticity of the driving laser pulse. To the best of our knowledge, the ELIED approach is the only successful method thus far for obtaining incident angle-resolved ionic MFDCS. Our results establish an intuitive interpretation to the complex elliptical laser-induced electron recollision dynamics and may provide new insights into the high-order above-threshold ionization and high-harmonic generations driven by elliptical laser pulses. ELIED has the potential to reveal the tomographic structural information of molecules with the femtosecond and subangstrom spatiotemporal resolution and also may have applications in molecular chirality discrimination.

[1] H. Fuest *et al.*, Phys. Rev. Lett. **122**, 053002 (2019).
[2] H. N. Chapman *et al.*, Nature (London) **470**, 73 (2011).
[3] M. M. Seibert *et al.*, Nature (London) **470**, 78 (2011).
[4] B. Wolter *et al.*, Science **354**, 308 (2016).
[5] J. Cao, H. Ihee, and A. H. Zewail, Proc. Natl. Acad. Sci. U.S.A. **96**, 338 (1999).
[6] J. C. Williamson, J. Cao, H. Ihee, H. Frey, and A. H. Zewail, Nature (London) **386**, 159 (1997).
[7] Y. Morimoto and P. Baum, Nat. Phys. **14**, 252 (2018).
[8] M. Meckel *et al.*, Science **320**, 1478 (2008).
[9] A. Sanchez *et al.*, Nat. Commun. **12**, 1520 (2021).
[10] M. P. Minitti *et al.*, Phys. Rev. Lett. **114**, 255501 (2015).
[11] J. M. Glownia *et al.*, Phys. Rev. Lett. **117**, 153003 (2016).
[12] Z. Vager, R. Naaman, and E. P. Kanter, Science **244**, 426 (1989).
[13] M. Pitzer *et al.*, Science **341**, 1096 (2013).
[14] P. Baum, D.-S. Yang, and A. H. Zewail, Science **318**, 788 (2007).
[15] Y. Liu *et al.*, Phys. Rev. X **10**, 021016 (2020).
[16] F. Qi *et al.*, Phys. Rev. Lett. **124**, 134803 (2020).
[17] R. Neutze and J. Hajdu, Proc. Natl. Acad. Sci. U.S.A. **94**, 5651 (1997).
[18] J. Feng *et al.*, Phys. Rev. Lett. **128**, 052501 (2022).
[19] H. Ibrahim *et al.*, Nat. Commun. **5**, 4422 (2014).
[20] R. Boll *et al.*, Nat. Phys. **18**, 423 (2022).
[21] M. Okunishi, H. Niikura, R. R. Lucchese, T. Morishita, and K. Ueda, Phys. Rev. Lett. **106**, 063001 (2011).
[22] D. Ray *et al.*, Phys. Rev. Lett. **100**, 143002 (2008).
[23] M. G. Pullen *et al.*, Nat. Commun. **7**, 11922 (2016).
[24] R. Sun, X. Lai, S. Yu, Y. Wang, S. Xu, W. Quan, and X. Liu, Phys. Rev. Lett. **122**, 193202 (2019).
[25] M. G. Pullen *et al.*, Nat. Commun. **6**, 7262 (2015).
[26] Y. Ito, M. Okunishi, T. Morishita, O. I. Tolstikhin, and K. Ueda, Phys. Rev. A **97**, 053411 (2018).
[27] Z. Chen, A.-T. Le, T. Morishita, and C. D. Lin, J. Phys. B **42**, 061001 (2009).
[28] C. D. Lin, A.-T. Le, Z. Chen, T. Morishita, and R. Lucchese, J. Phys. B **43**, 122001 (2010).
[29] J. Xu, Z. Chen, A.-T. Le, and C. D. Lin, Phys. Rev. A **82**, 033403 (2010).
[30] K. Hoshina, K. Yamanouchi, T. Ohshima, Y. Ose, and H. Todokoro, Chem. Phys. Lett. **353**, 27 (2002).
[31] K. Hoshina, K. Yamanouchi, T. Ohshima, Y. Ose, and H. Todokoro, Chem. Phys. Lett. **353**, 33 (2002).
[32] P. Reckenthaeler, M. Centurion, W. Fuß, S. A. Trushin, F. Krausz, and E. E. Fill, Phys. Rev. Lett. **102**, 213001 (2009).
[33] Y. Yang, H. Ren, M. Zhang, S. Zhou, X. Mu, X. Li, Z. Wang, K. Deng, M. Li, P. Ma *et al.*, Nat. Commun. **14**, 4951 (2023).
[34] See Supplemental Material at http://link.aps.org/supplemental/10.1103/PhysRevLett.133.113203, which includes Refs. [35–40], for additional information about the experimental method and detailed discussion from other works related to our result.
[35] J. Ullrich, R. Moshammer, A. Dorn, R. Dörner, L. P. H. Schmidt, and H. Schmidt-Böcking, Rep. Prog. Phys. **66**, 1463 (2003).
[36] C. Wang, X. Li, X.-R. Xiao, Y. Yang, S. Luo, X. Yu, X. Xu, L.-Y. Peng, Q. Gong, and D. Ding, Phys. Rev. Lett. **122**, 013203 (2019).
[37] D. Shafir, H. Soifer, C. Vozzi, A. S. Johnson, A. Hartung, Z. Dube, D. M. Villeneuve, P. B. Corkum, N. Dudovich, and A. Staudte, Phys. Rev. Lett. **111**, 023005 (2013).
[38] D. Comtois, D. Zeidler, H. Pépin, J. C. Kieffer, D. M. Villeneuve, and P. B. Corkum, J. Phys. B **38**, 1923 (2005).
[39] N. Kaya, G. Kaya, M. Sayrac, Y. Boran, S. Anumula, J. Strohaber, A. Kolomenskii, and H. Schuessler, Opt. Express **24**, 2562 (2016).
[40] B. Efron, SIAM. Rev. Soc. Ind. Appl. Math **21**, 460–480 (1979).

[41] C. I. Blaga, J. Xu, A. D. DiChiara, E. Sistrunk, K. Zhang, P. Agostini, T. A. Miller, L. F. DiMauro, and C. D. Lin, Nature (London) **483**, 194 (2012).

[42] P. B. Corkum, Phys. Rev. Lett. **71**, 1994 (1993).

[43] B. Belsa *et al.*, Struct. Dyn. **8**, 014301 (2021).

[44] J.-L. Bégin, M. Alsaawy, and R. Bhardwaj, Sci. Rep. **10**, 14074 (2020).

[45] K. Ray, S. P. Ananthavel, D. H. Waldeck, and R. Naaman, Science **283**, 814 (1999).

[46] X. Wang and J. H. Eberly, Phys. Rev. A **86**, 013421 (2012).

[47] T. Morishita, A.-T. Le, Z. Chen, and C. D. Lin, Phys. Rev. Lett. **100**, 013903 (2008).

[48] M. Okunishi, T. Morishita, G. Prümper, K. Shimada, C. D. Lin, S. Watanabe, and K. Ueda, Phys. Rev. Lett. **100**, 143001 (2008).

[49] G. G. Paulus, W. Becker, W. Nicklich, and H. Walther, J. Phys. B **27**, L703 (1994).

[50] A. W. Bray, S. Eckart, and A. S. Kheifets, Phys. Rev. Lett. **121**, 123201 (2018).

[51] X. Hu, C.-Z. Gao, Z. Chen, J. Wang, Y. Wu, and Y. Wang, Phys. Rev. A **96**, 052701 (2017).

[52] X. Hu, C.-Z. Gao, W.-J. Ma, J. Wang, and Y. Wu, J. Phys. B **52**, 105202 (2019).

[53] I. V. Litvinyuk, K. F. Lee, P. W. Dooley, D. M. Rayner, D. M. Villeneuve, and P. B. Corkum, Phys. Rev. Lett. **90**, 233003 (2003).

[54] D. Pavičić, K. F. Lee, D. M. Rayner, P. B. Corkum, and D. M. Villeneuve, Phys. Rev. Lett. **98**, 243001 (2007).

[55] M. Gong, X. Li, S. B. Zhang, S. Niu, X. Ren, E. Wang, A. Dorn, and X. Chen, Phys. Rev. A **98**, 042710 (2018).